Nanoscale Advances

ROYAL SOCIETY OF CHEMISTRY

PAPER

View Article Online
View Journal | View Issue

Cite this: *Nanoscale Adv.*, 2025, **7**, 5580

Collective motion of methylammonium cations affects phase transitions and self-trapped exciton emission in A-site engineered $MAPbI_3$ films

Chia-Hsun Yeh,[a] Wen-Yu Cheng,[bc] Tai-Che Chou,[a] Yi-Chun Liu,[a] Chia-Wei Chang,[a] Yu-Sheng Chen,[d] Chih-Hsing Wang,[a] Shih-Chang Weng,[d] Ian D. Sharp, *[bc] Pi-Tai Chou [ae] and Chang-Ming Jiang *[ae]

Hybrid organic–inorganic halide perovskites are celebrated for their exceptional optoelectronic properties and facile fabrication processes, making them prime candidates for next-generation photovoltaic and optoelectronic devices. By incorporating larger organic cations at the A-site, a novel class of '3D hollow perovskites' has been developed, exhibiting enhanced stability and tunable optoelectronic properties. This study systematically explores the structural, phase transition, and photophysical characteristics of {en}$MAPbI_3$ thin films with varying ethylenediammonium (en^{2+}) content. The incorporation of less polar en^{2+} expands the perovskite unit cell, prolongs carrier lifetimes, and disrupts MA^+ dipole–dipole interactions, thereby lowering the tetragonal-to-orthorhombic phase transition temperature. Temperature-dependent photoluminescence studies reveal that en^{2+} incorporation reduces the intensity and Stokes shift of self-trapped exciton emission at low temperatures, which are attributed to the diminished collective rotational dynamics of MA^+ cations. These findings underscore the critical role of A-site cation dynamics in modulating phase stability and excitonic behaviour within hybrid halide perovskites, deepening our understanding of the interplay between organic cations and the inorganic framework and highlighting the potential of 3D hollow perovskites for stable and tunable optoelectronic applications.

Received 17th June 2025
Accepted 25th July 2025

DOI: 10.1039/d5na00599j

rsc.li/nanoscale-advances

Introduction

Hybrid organic–inorganic halide perovskites, such as methylammonium lead iodide ($MAPbI_3$), have emerged as promising materials for next-generation optoelectronic devices due to their exceptional properties, including long carrier lifetimes, large absorption coefficients, tuneable band gaps, and intrinsic defect tolerance.[1–5] These attributes have propelled the power conversion efficiencies (PCEs) of single-junction perovskite solar cells to beyond 25%.[6–8] However, the inherent instability of halide perovskites under ambient conditions, including due to the volatility of organic cations, remains a critical challenge for large-scale deployment.[9–11] Moreover, efforts to replace toxic Pb^{2+} with Sn^{2+} exacerbate these instability issues and lead to much lower achievable PCEs.[12]

To address these limitations, a new family of "3D hollow perovskites," described by the general formula $(L)_x(A)_{1-x}BX_3$, has recently been introduced. In these systems, larger organic cations (L), such as ethylenediammonium (en^{2+}) and hydroxyethylammonium (HEA^+), partially replace methylammonium (MA^+) or formamidinium (FA^+) at the A-site, with B = Pb^{2+} or Sn^{2+}, and X = Br^- or I^-.[13–23] These materials exhibit enhanced air and photostability, alongside desirable photovoltaic performance characteristics, in both Pb- and Sn-based systems. For example, mixed-halide perovskite such as $Cs_{0.17}FA_{0.83}Pb(I_{0.6}Br_{0.4})_3$ often suffers from halide segregation under continuous illumination, but the addition of en^{2+} significantly suppresses the mobility of halide vacancies and improves chemical stability.[17] Similarly, replacing 10% propylenediammonium and trimethylenediammonium into the A-site of $FASnI_3$ has been reported to increase the power conversion efficiency from 2.53% to 5.85% and 5.53%, respectively.[20]

Importantly, the incorporation of these larger organic cations modifies the perovskite crystal structure in two key ways: (1) by expanding the unit cell and, in some cases, inducing phase transitions, as governed by the Goldschmidt tolerance factor,[24,25] and (2) through the creation of vacancies at the B-site

[a]*Department of Chemistry, National Taiwan University, 10617 Taipei, Taiwan. E-mail: cmjiang@ntu.edu.tw*
[b]*Walter Schottky Institute, Technical University of Munich, 85748 Garching, Germany. E-mail: sharp@wsi.tum.de*
[c]*Physics Department, TUM School of Natural Sciences, Technical University of Munich, 85748 Garching, Germany*
[d]*National Synchrotron Radiation Research Center, 300092 Hsinchu, Taiwan*
[e]*Center for Emerging Materials and Advanced Devices, National Taiwan University, 10617 Taipei, Taiwan*

and halide positions to accommodate the larger cations, forming a robust 3D hollow framework.[14,16,18,19] These structural changes not only improve material stability but also allow for tuning of the optoelectronic properties, including by widening optical bandgaps and extending carrier lifetimes, despite the introduction of additional vacancy defects.[15,18,19] Nevertheless, the fundamental mechanisms by which these larger cations influence carrier dynamics and excitonic behaviour remain elusive.

The dynamic behaviour of A-site cations, including their anisotropic sizes and roles as hydrogen bond donors, plays a pivotal role in determining the structural and optoelectronic properties of hybrid halide perovskites.[26–28] Despite the absence of covalent bonding between organic and inorganic components, A-site cations, such as MA^+, significantly influence phase transitions and excitonic behaviour through their rotational dynamics and dipole interactions. For example, $MAPbI_3$ undergoes distinct phase transitions–from cubic to tetragonal to orthorhombic phases–as the temperature decreases, as reflected by the tilting of $[PbI_6]$ octahedra.[29–32] At low temperatures, the diminished rotational degrees of freedom of MA^+ result in organized domains defined by dipole–dipole interactions between MA^+, manifesting in the antiparallel arrangement of MA^+ dipoles between adjacent $MAPbI_3$ layers.[19] These dipole–dipole interactions, alongside hydrogen bonding between MA^+ and I^-, drive lattice distortions and phase transitions. Moreover, hybrid halide perovskites comprising other organic cations show similar behaviour. For example, neutron scattering studies have revealed that the isotropic orientation of formamidinium (FA^+) in the high-temperature cubic phase of $FAPbI_3$ becomes frozen into an ordered arrangement in the low-temperature tetragonal phase, signifying the interplay between organic cation rotational dynamics and the inorganic framework.[33] Recent studies have also demonstrated that the structural dynamics in hybrid halide perovskites facilitate self-trapped exciton (STE) formation through strong electron–phonon coupling, a characteristic feature of highly ionic halide perovskites.[34–37] Unlike free excitons, which recombine comparatively rapidly, STEs are stabilized by lattice distortions, resulting in prolonged carrier lifetimes and broadband emission.[37–40] However, the extent to which A-site cation rotational dynamics influence STE formation and phase stabilities is still poorly understood.

Motivated by these challenges, this study investigates the structures, phase transitions, and photophysical properties of 3D hollow {en}$MAPbI_3$ thin films with varying en^{2+} content. The much lower static dipole moment of en^{2+} compared to MA^+ disrupts long-range dipole–dipole interactions among A-site cations, which alters phase transition temperatures and carrier recombination dynamics. Using temperature-dependent photoluminescence (PL) and X-ray diffraction (XRD), we reveal how en^{2+} incorporation suppresses the tetragonal-to-orthorhombic perovskite (TP-to-OP) phase transition and reduces the intensity and Stokes shift of STE emission at low temperatures. These insights bridge the gap between structural dynamics and carrier behaviour in hybrid halide perovskites, offering a pathway for optimizing these compounds for photovoltaic and light-emitting diode applications.

Experimental methods

Synthesis of {en}$MAPbI_3$ films

All films were prepared on amorphous SiO_2 substrates (fused silica, 1 × 1 cm^2) using a one-step spin-coating procedure in a nitrogen-filled glove box (Fig. S1). For pristine $MAPbI_3$, a precursor solution was prepared by dissolving 0.8 mmol of methylammonium iodide (CH_3NH_3I, >99%, TCI) and 0.8 mmol of lead(II) iodide (PbI_2, 99.999%, Alfa Aesar) in 1.00 mL of a 4 : 1 (v/v) DMF/DMSO mixture. {en}$MAPbI_3$ films were synthesized by partially replacing CH_3NH_3I with ethylenediammonium iodide ($C_2H_8N_2 \cdot 2HI$, >98%, Sigma-Aldrich) at the specified stoichiometric ratio to achieve en^{2+} substitution of 5.0, 7.5, 10.0, and 15.0%.

The fused silica substrates were cleaned sequentially in an ultrasonic bath with deionized water (10 min, twice), acetone (20 min), and isopropanol (20 min). After drying, first with a nitrogen stream and then in an oven at 80 °C for 8 h, the substrates were treated in a UV-ozone cleaner for 20 min. The spin-coating process was performed using 10 μL of precursor solution at 4000 rpm for 30 s, with an acceleration rate of 800 rpm s^{-1}. At a time of 3 s before the spin-coating process ended, 100 μL of chlorobenzene (anhydrous, 99.9%, Sigma-Aldrich) anti-solvent was dropped onto the rotating substrate. The as-coated films were then annealed on a hotplate at optimized temperatures for 10 min (see SI for details). A protective layer was subsequently applied by spin-coating 15 μL of a 10 mg mL^{-1} poly(methyl methacrylate) (PMMA) solution in chlorobenzene at 5000 rpm for 35 s (800 rpm per s acceleration rate), followed by annealing at 80 °C for 10 min.

Morphological and structural characterization

The surface morphologies of $MAPbI_3$ and {en}$MAPbI_3$ films were examined using a field emission scanning electron microscope (JSM-7600F, JEOL) in secondary electron detection mode. Room-temperature powder X-ray diffraction (PXRD) patterns were recorded using a PANalytical X'Pert PRO diffractometer equipped with a Cu anode ($\lambda_{K\alpha} = 1.54178$ Å) over a θ–2θ range of 5–50°. Temperature-dependent XRD measurements were performed at Beamline 09A of the Taiwan Photon Source, National Synchrotron Radiation Research Center. For this measurement, the thin-film sample was placed in a closed-cycle helium cryostat mounted on the Eulerian cradle of a 9-circle diffractometer, and a scintillation detector on the 2θ arm was used for XRD measurement using an X-ray energy of 12 keV (λ = 1.0332 Å). The sample temperature was controlled between 20–300 K, with a stabilization time of 15 min at each temperature point.

Steady-state and time-resolved optical characterization

Ultraviolet-visible (UV-Vis) transmission spectra of $MAPbI_3$ and {en}$MAPbI_3$ films were recorded over the wavelength range of 400–1200 nm using a spectrophotometer (UH-5700, Hitachi)

with a bare fused silica substrate as the reference. Photoluminescence (PL) spectra were measured using a fluorimeter (FLS 980, Edinburgh Instruments) equipped with a photomultiplier tube as the detector and a 510 nm pulsed laser diode as the excitation source. The temporal evolution of the PL intensity was analysed using the time-correlated single photon counting (TCSPC) technique. The instrument response function, obtained with aluminium foil at the sample mount, was deconvoluted from the time-resolved PL traces.

For low-temperature PL measurements, thin-film samples were mounted in a closed-cycle helium cryostat (CS202-DMX-1AL, Advanced Research Systems, Inc.) evacuated by a turbomolecular pump. A thermocouple installed on the cold finger of the cryostat was connected to a temperature controller (Model 350, Lake Shore), which was used to adjust the sample temperature between 10–300 K using an integrated resistive heater.

Results and discussion

Structural analysis of {en}$MAPbI_3$ films

The structural properties of {en}$MAPbI_3$ thin films with 0–15% en^{2+} incorporation were first investigated *via* powder X-ray diffraction (PXRD). As shown in Fig. 1a, all diffraction peaks below 10% en^{2+} loading can be indexed to the tetragonal perovskite structure (TP; space group $I4/mcm$). Two trends were observed with increasing en^{2+} loading: (1) a monotonic shift of all diffraction peaks toward smaller 2θ angles (Fig. 1b), indicating unit cell expansion due to the incorporation of larger en^{2+}, consistent with prior reports of {en}$MAPbI_3$ (ref. 30, 32 and 36) and similar hollow hybrid halide perovskites;[16] and (2) reduced diffraction intensities and slightly increased peak widths. To further assess structural disorder, we plot the full width at half maximum (FWHM) of the $MAPbI_3$ (110) diffraction peak as a function of en^{2+} content (Fig. 1c). A steady increase in FWHM from 0.07° for pristine $MAPbI_3$ to 0.14° for the 15% en^{2+} film support a trend of increasing lattice disorder. While the reduced diffraction intensities may also arise from variation in film thickness – as suggested by the progressively decreasing optical density in UV-Vis absorption spectra (Fig. 2a) – the increased FWHM values provide direct evidence of disrupted long-range crystallographic order in {en}$MAPbI_3$.

Notably, partial substitution of MA^+ with the larger en^{2+} cation can give rise to additional low-angle diffraction peaks below $2\theta = 10°$ (Fig. S2). Such features are often attributed either to the formation of quasi-2D $MAPbI_3$ domains, commonly observed when long-chain organic cations are introduced during synthesis,[21,24] or to transient, solvent-containing intermediate phases. In our case, these low-angle peaks were largely suppressed through careful optimization of the spin-coating and annealing conditions. The absence of both low-angle features and PbI_2 impurity peaks in the PXRD patterns (Fig. S2) confirms the successful preparation of 3D hollow {en}$MAPbI_3$ thin films. Additionally, SEM reveals that all samples exhibited compact, continuous films on fused silica substrates, with film thicknesses of approximately 230 nm (Fig. S3 and S4).

Interestingly, the (211) diffraction peak of tetragonal $MAPbI_3$ weakens at 10% en^{2+} loading and disappears entirely at 15% en^{2+} loading. While the PXRD peak broadening in our thin films prevents full resolution of the (110)/(220) doublets and precludes reliable unit cell refinement, the observed disappearance of the (211) reflection combined with photophysical trends (*vide infra*) supports the assignment of a tetragonal-to-cubic phase (CP; space group $Pm\bar{3}m$) transition with increasing en^{2+} incorporation. This transition aligns with the prediction from the Goldschmidt tolerance factor and previous reports,[16,41] indicating that incorporating larger en^{2+} cations stabilizes the cubic phase at room temperature.

Photophysical properties and carrier dynamics

The UV-Vis absorption spectra of {en}$MAPbI_3$ films (Fig. 2a) exhibit a systematic blueshift in the absorption onset with increasing en^{2+} loading, indicative of a widening optical bandgap. Room-temperature PL spectra (Fig. 2b), recorded under 510 nm ($h\nu = 2.43$ eV) excitation, show a single emission peak attributed to the radiative recombination of free carriers.[42] This PL peak shifts from 1.58 eV for pristine $MAPbI_3$ to 1.65 eV for the 15% en^{2+} sample, reflecting bandgap widening due to lattice expansion. The bandgap modification arises from the

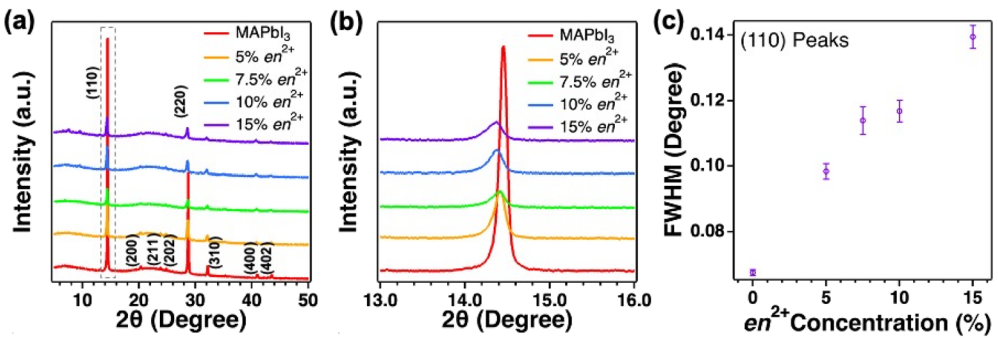

Fig. 1 (a) PXRD patterns of {en}$MAPbI_3$ films with different en^{2+} loadings. (b) Enlarged PXRD patterns around the $MAPbI_3$ (110) diffraction peak as enclosed by the grey dashed box in panel (a). (c) The change of the full width at half maxima of the tetragonal $MAPbI_3$ (110) reflection with en^{2+} loadings.

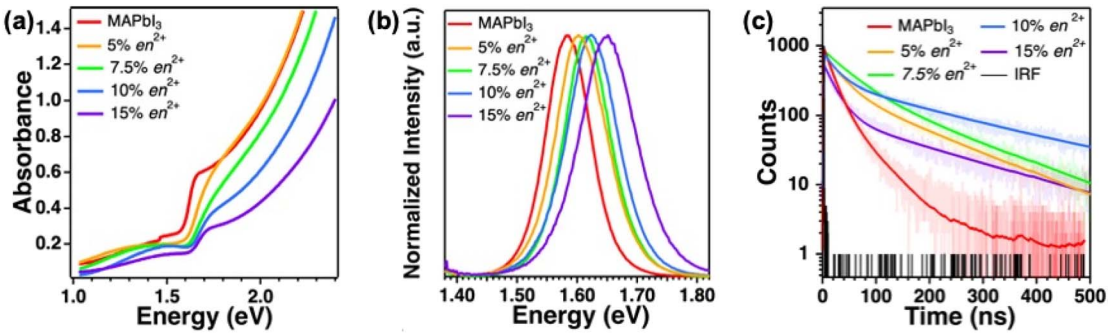

Fig. 2 (a) UV-Vis absorption spectra, (b) room-temperature steady-state PL spectra, and (c) time-resolved PL traces measured from {en}$MAPbI_3$ films with different en^{2+} loadings. The solid lines in panel (c) represent the fitting results using a bi-exponential model convoluted with the instrument response function.

reduced energy of the Pb 6s–I 5p anti-bonding valence band maximum (VBM) as the unit cell expands, while the conduction band minimum (CBM), having non-bonding character, remains unaffected.[36,43] These results confirm that en^{2+} incorporation not only modifies the structural properties of $MAPbI_3$ but also tunes its optoelectronic properties.

Time-correlated single-photon counting (TCSPC) measurements provide insights into carrier dynamics of {en}$MAPbI_3$ films (Fig. 2c). PL decay traces were fitted using a bi-exponential model:

$$I(t) = A_0 + A_1 \exp\left(-\frac{t}{\tau_1}\right) + A_2 \exp\left(-\frac{t}{\tau_2}\right) \quad (1)$$

where A_0 is the background level, A_i is the weighting factor for each decay channel, and τ_i is the decay time. Here, τ_1 represents Schottky–Read–Hall recombination mediated by defect states, while τ_2 corresponds to band-to-band radiative recombination of free carriers at room temperature.[42,44] The fitting results (Table 1) reveal a significant increase in τ_2 with en^{2+} loading, except for the 15% en^{2+} sample, where the trend reverses. Concurrently, the ratio $A_1/(A_1 + A_2)$ decreases from 0.80 for pristine $MAPbI_3$ to 0.62 for the 10% en^{2+} sample, indicating suppression of defect-mediated non-radiative recombination pathways in 3D hollow {en}$MAPbI_3$. The intensity-weighted average PL lifetime (τ_{avg}) was calculated as.

$$\tau_{avg} = \frac{A_1\tau_1^2 + A_2\tau_2^2}{A_1\tau_1 + A_2\tau_2} \quad (2)$$

Here, τ_{avg} increased from 30.5 ns for pristine $MAPbI_3$ to 172.0 ns for the 10% en^{2+} film, consistent with prolonged carrier lifetimes observed in structurally similar {en}$FASnI_3$, {en}$FA_{0.5}MA_{0.5}Pb_{0.5}Sn_{0.5}I_3$, and {en}$MASnI_3$ films.[14,18,19] At higher en^{2+} loadings, however, the emergence of the cubic $MAPbI_3$ phase disrupts these trends. It has been reported that the CP phase of $MAPbI_3$ exhibits lower electrical conductivity and more pronounced defect-mediated recombination than the TP phase,[29] aligning with shortened τ_1 and increased $A_1/(A_1 + A_2)$ ratio in films with 15% en^{2+} loading. Accordingly, τ_{avg} decreased significantly to 127.0 ns for the 15% en^{2+} film.

Phase transition behaviours

Temperature-dependent PL spectra of {en}$MAPbI_3$ thin films (Fig. 3) reveal redshifts in emission peaks as the temperature decreases from 300 K. Such a redshift has been previously observed and can be attributed to a unit cell contraction that elevates the Pb–I anti-bonding energy levels at the VBM.[44] For pristine $MAPbI_3$, a sudden blueshift in the PL at 150 K corresponds to the TP-to-OP transition, during which the tilting of $[PbI_6]$ octahedra weakens the interaction between Pb^{2+} and I^-. To provide further evidence for the TP-to-OP transition, temperature-dependent XRD was conducted on a pristine $MAPbI_3$ film (Fig. S5). Here, the (110) diffraction of TP and the (101) diffraction of OP were fitted using a Voigt function, and their peak positions were plotted as functions of temperature. In general, the diffraction peaks shifted to lower 2θ angles as the temperature increased, consistent with the assignment that the expanded unit cell is responsible for the PL redshift with decreasing temperature. In addition, a distinct change in the slopes of the diffraction peak positions over the 130–170 K

Table 1 Fitting results for the time-resolved PL traces monitored at the respective peak PL emission energies of {en}$MAPbI_3$ films with varying en^{2+} loadings

Samples	PL peak (eV)	τ_1 (ns)	A_1	τ_2 (ns)	A_2	τ_{avg} (ns)	$A_1/(A_1 + A_2)$
$MAPbI_3$	1.58	16.5 ± 0.2	0.082 ± 0.001	49.6 ± 0.7	0.020 ± 0.001	30.5	0.80
5% en^{2+}	1.60	29.4 ± 0.6	0.188 ± 0.002	136.9 ± 1.1	0.084 ± 0.001	102.0	0.69
7.5% en^{2+}	1.61	46.9 ± 0.9	0.197 ± 0.003	148.4 ± 1.5	0.096 ± 0.003	108.5	0.67
10% en^{2+}	1.62	23.7 ± 0.4	0.071 ± 0.001	200.9 ± 1.3	0.043 ± 0.001	172.0	0.62
15% en^{2+}	1.65	21.7 ± 0.4	0.157 ± 0.002	185.6 ± 1.8	0.033 ± 0.001	127.0	0.83

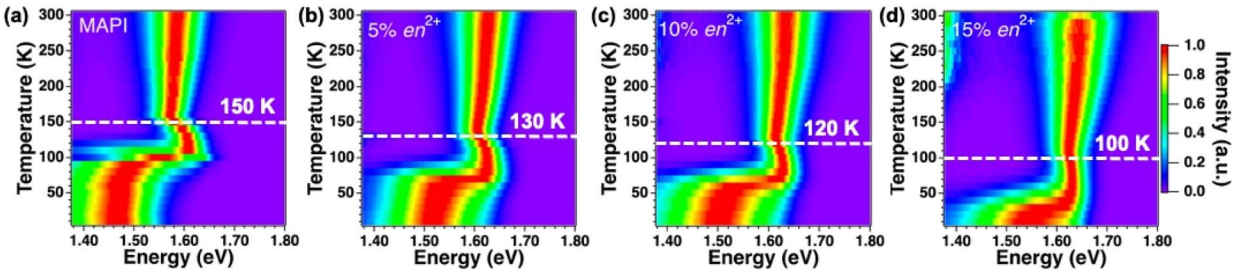

Fig. 3 Temperature-dependent PL spectra of (a) pristine $MAPbI_3$ and {en}$MAPbI_3$ films with (b) 5%, (c) 10%, and (d) 15% en^{2+} loading. The tetragonal-to-orthorhombic phase transition temperatures are marked with dashed lines.

range verified the TP-to-OP phase transition, consistent with the temperature-dependent PL measurement. Finally, increasing en^{2+} loading was found to lower the phase transition temperature observed by PL to 130 K, 120 K, and 100 K for films with 5%, 10%, and 15% en^{2+}, respectively, suggesting enhanced TP stability due to en^{2+} incorporation.

Based on the temperature-dependent PL and XRD results, we find that the TP-to-OP phase transition temperature decreases as the en^{2+} loading in 3D hollow perovskite increases. We hypothesize that this phenomenon originates from the smaller molecular dipole moments of en^{2+} cations compared to MA^+. Indeed, prior computational studies on $MAPbI_3$ have revealed that dipole–dipole interactions give rise to an ordered arrangement of MA^+ cations, which is the primary driving force for the TP-to-OP phase transition at low temperatures.[27] The random incorporation of the less polar en^{2+} cation at the A-site would disrupt such collective motion of MA^+ and, consequently, require a further reduction of the lattice temperature to induce MA^+ ordering and to initiate the transition to the OP phase.

Electron–phonon coupling in {en}$MAPbI_3$

The full widths at half maximum (FWHMs) of PL emission peaks in the TP temperature range were analysed to provide insight into the coupling between electrons and longitudinal optical (LO) phonons, as well as the intrinsic disorder, in {en}$MAPbI_3$ (Fig. 4). In the weak electron–phonon coupling regime, the temperature-dependent PL linewidth (Γ) can be described by:

$$\Gamma(T) = \Gamma_0 + \gamma_{LO}\left(\frac{1}{e^{\frac{E_{LO}}{k_B T}} - 1}\right) \quad (3)$$

where Γ_0 is the intrinsic linewidth, and E_{LO} and γ_{LO} are the energy and coupling constant associated with the LO phonons, respectively.[45,46] Here, E_{LO} was fixed as 11.5 meV, an experimental value previously extracted from $MAPbI_3$.[45] Fitting results (Table 2) reveal consistent 17–22 meV electron–phonon coupling strengths across all films. However, Γ_0 can be seen to increase progressively with en^{2+} cation loading, consistent with the greater lattice disorder in 3D hollow {en}$MAPbI_3$ films with a higher extent of en^{2+} incorporation.

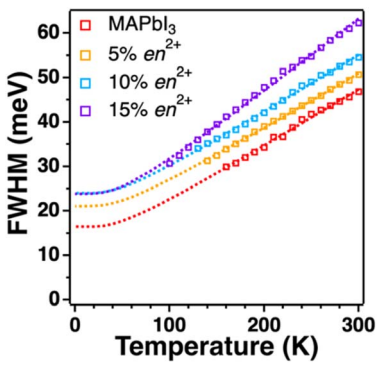

Fig. 4 The change of PL linewidths of {en}$MAPbI_3$ films as a function of temperature. The dotted lines represent the fitting results obtained in the weak electron–phonon coupling limit, as described in the main text.

Self-trapped exciton (STE) formation

Importantly, temperature-dependent PL spectra reveal the emergence of broadband emission far below the TP-to-OP transition temperature, especially for the pristine $MAPbI_3$ film (Fig. 3). A comparison of 10 K PL spectra obtained from {en}$MAPbI_3$ reveals a blueshift of this feature with increasing en^{2+} cation content (Fig. S6). Furthermore, as the en^{2+} cation loading increases in 3D hollow {en}$MAPbI_3$, the temperature at which the broadband emission feature appears becomes lower, and the Stokes shifts become reduced. The large Stokes shifts of these emission features preclude their origin as being from the recombination of free excitons, which typically exhibit binding energies of < 20 meV in $MAPbI_3$ single crystals and thin films.[47,48] Rather, these low-temperature PL features in hybrid halide perovskites have been widely attributed to one of two

Table 2 List of intrinsic PL linewidths Γ_0 and electron–phonon coupling strengths γ_{LO} for {en}$MAPbI_3$ films with different en^{2+} cation loadings. In all cases, a value of E_{LO} of 11.5 meV was used, as described in the text

Samples	Γ_0 (meV)	γ_{LO} (meV)
$MAPbI_3$	16.5 ± 0.5	17.3 ± 0.4
5% en^{2+}	21.1 ± 0.2	16.7 ± 0.1
10% en^{2+}	24.0 ± 0.3	17.4 ± 0.2
15% en^{2+}	23.9 ± 0.3	22.0 ± 0.3

mechanisms: defect-related (donor–acceptor pair transition) or self-trapped exciton emission.[31,37,49–52]

To differentiate these radiative recombination pathways, excitation power-dependent PL measurements were performed for the pristine $MAPbI_3$ film at 160 K (Fig. 5a and b), where free carrier recombination dominates, and at 10 K (Fig. 5c and d), where the broadband emission with a large Stokes shift dominates. In both cases, the integrated PL intensities exhibited a linear relationship with the excitation power density. As defect-related emission is expected to saturate at higher excitation powers due to finite defect concentrations, which was not observed here, we conclude that the broad low-temperature emission originates from STEs in the OP phase rather than radiative recombination at defect states. Further evidence of this STE origin is the monotonic blueshift of the 10 K PL peak with increasing excitation power density, which is not expected for PL associated with free carriers, free excitons, or defects. For example, the PL peak of pristine $MAPbI_3$ shifted from 1.45 eV to 1.48 eV as the excitation power density increased from 0.7 mW cm^{-2} to 6.4 mW cm^{-2} (Fig. 5d), a trend similarly observed for the 7.5% en^{2+} film (Fig. S7). We note that the 10^{15}–10^{16} cm^{-3} excitation carrier densities used in this study are well below the 10^{17}–10^{18} cm^{-3} regime where the band-filling effect is typically observed in $MAPbI_3$,[53,54] and no blueshift is seen in the free exciton emission at higher temperatures (Fig. 5a). Therefore, we attribute the blueshifting of the low-temperature broadband emission to the reduction of the STE domain size at higher excitation powers, rather than to band-filling.

The formation of STEs involves the interaction between free excitons (FEs) and the surrounding lattice. We posit that the driving force for STE formation primarily arises from the collective motion of MA^+ cations surrounding FEs, rather than the distortions in the inorganic $[PbI_6]$ framework. Just below the TP-to-OP phase transition temperature, FE emission dominates the PL spectra, with MA^+ dipoles aligned within the same plane but antiparallel to the adjacent $MAPbI_3$ layers, as indicated by prior molecular dynamics simulations.[27] At lower temperatures, MA^+ cations surrounding the FE realign to accommodate the excitonic dipole moment, subsequently inducing distortions in the corner-sharing $[PbI_6]$ octahedra and stabilizing STE (Fig. 6a). This process resembles the reorganization of polar solvent molecules around charged species to reach a new equilibrium configuration with lower free energy. Greater

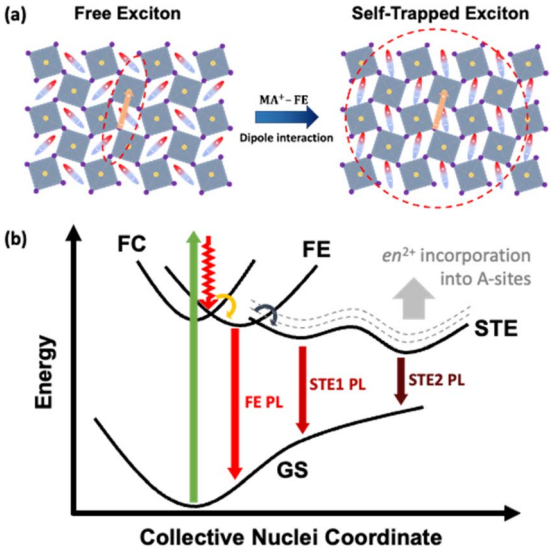

Fig. 6 (a) Illustrative diagram for the formation of a self-trapped exciton at low temperatures through the collective rearrangement of methylammonium cations in the orthorhombic phase of $MAPbI_3$. (b) Potential energy diagram for the sequential evolution from the free carrier (FC) excited state to the free exciton (FE) state and, finally, to the self-trapped exciton (STE) state.

displacement of the collective nuclear coordinates corresponds to stronger stabilization, manifesting as larger Stokes shifts for STE emission relative to FE emission (Fig. 6b).

Under low excitation power, each FE can couple to a greater number of MA^+ cations, leading to more extensive lattice distortions and larger Stokes shifts. Conversely, higher excitation powers generate larger densities of FEs, limiting the extent of lattice distortion and resulting in smaller energy stabilization. This behaviour explains the excitation power-dependent PL peak position at low temperatures for $MAPbI_3$ and {en} $MAPbI_3$ films. Furthermore, the differences in PL spectral profiles obtained with different excitation sources, as shown in Fig. S8, support this interpretation. For both pristine $MAPbI_3$ and the 7.5% en^{2+} film, excitation with a xenon lamp source (monochromated at 510 nm, continuous wave) produced significantly more redshifted PL spectra compared to a pulsed laser source due to the significantly lower excitation power density (~0.15 mW cm^{-2}) provided by the xenon lamp.

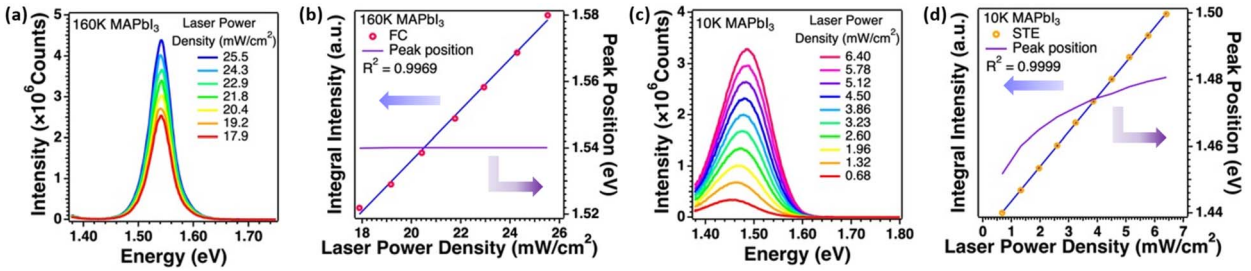

Fig. 5 Steady-state PL spectra measured from a pristine $MAPbI_3$ film at (a) 160 K and (c) 10 K using different excitation powers from a 510 nm pulsed laser. The integrated PL emission intensities and the emission peak positions for free carriers (FC) and self-trapped exciton (STE) are plotted as a function of the excitation power in (b) and (d), respectively.

In 3D hollow $MAPbI_3$ films, the suppression of STE formation is primarily attributed to disrupted MA^+ dipole–dipole interactions rather than to significant changes in intrinsic electron–phonon coupling strength. While the fitted electron–phonon coupling parameter γ_{LO} remains nearly constant up to 10% en^{2+} incorporation (Table 2), the introduction of less polar en^{2+} cations interrupts the collective MA^+ dynamics that are critical for stabilizing STEs. This manifests as smaller Stokes shifts and less favourable competition with FE emission. Additionally, since STE formation is driven by MA^+ motion, higher en^{2+} content requires lower temperatures for STE emission to appear in {en}$MAPbI_3$, consistent with our experimental observations. At 90 K, the PL spectrum of pristine $MAPbI_3$ can be deconvoluted into three Gaussian peaks, corresponding to one FE and two STE emissions (Fig. 7a).

The presence of two distinct STE peaks suggests the existence of multiple local minima in the exciton-lattice potential energy surface, as illustrated in Fig. 6b. These may correspond to different configurations of MA^+ dipole orientations and $[PbI_6]$ octahedral distortions surrounding the self-trapped STE. Such variation in stabilization energies could also arise from heterogeneity in local lattice environments, especially in polycrystalline films. While the precise structural origins of the dual STE states remain to be resolved, this phenomenon is consistent with the interplay between organic dipole reorganization and inorganic lattice relaxation that governs STE formation.

TCSPC measurements were conducted to measure the temporal evolution at 780 nm and 850 nm (Fig. 7b and c). Here, the FE emission exhibited a much faster decay than the STE emission. More importantly, the rise of STE emission coincided with the fast decay component of the FE emission on the few-nanosecond timescale, signifying the collective rotational dynamics of MA^+ cations. For the {en}$MAPbI_3$ film with 7.5% en^{2+} loading, the steady-state PL spectrum at 90 K also consists of one FE and two STE emission features, though individual components are blue-shifted compared to the pristine $MAPbI_3$ (Fig. 7d). Similarly, the decay of the PL trace at 770 nm, with a major contribution from FE emission, matches the rise time of the STE-dominant PL trace at 870 nm (Fig. 7e and f). Nevertheless, we note that the broad STE emissions prevent the complete deconvolution of the FE emission kinetics, especially in 3D hollow {en}$MAPbI_3$ films with smaller Stokes shifts for the STE emission.

We also note that the broad low-energy $MAPbI_3$ emission observed at low temperatures has previously been attributed to donor–acceptor (DAP) transitions,[31,51] which can also exhibit a spectral blueshift with increasing excitation powers – consistent with our observations. However, we found that incorporation of en^{2+} into $MAPbI_3$ leads to a blueshift of both the orthorhombic-phase free exciton PL and the broadband emission (Fig. 3 and S6). For DAP transitions associated with point defects, the donor and acceptor levels are less likely to change in the 3D hollow $MAPbI_3$ structure. In contrast, prior molecular dynamics simulations suggest that MA^+ disorder in the orthorhombic phase can give rise to low-temperature broadband PL that blueshifts with increasing excitation power,[55] supporting our assignment of this feature to STE emission. Overall, the A-site cation engineering strategy employed here provides a unique means to modulate MA^+ dipole–dipole interactions, thereby tuning both the phase transition behaviour and the photophysical properties of hybrid halide perovskites.

Conclusions

This study investigates the structural and optical properties of {en}$MAPbI_3$, a 3D hollow halide perovskite, focusing on the

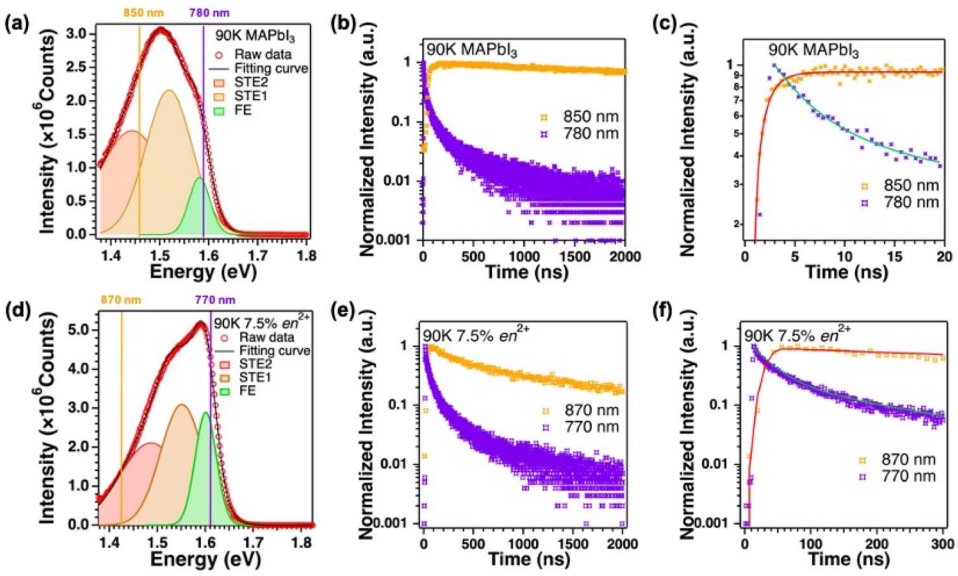

Fig. 7 Steady-state PL spectra of (a) pristine $MAPbI_3$ and (d) {en}$MAPbI_3$ with 7.5% en^{2+} loading, measured at 90 K using 510 nm excitation. For each sample, the time-resolved PL traces were monitored at two wavelengths to track the dynamics of (b and c) FE and (e and f) STE emissions, respectively.

effects of incorporating less polar en^{2+} cations at the A-sites. The larger size of en^{2+} compared to MA^+ leads to unit cell expansion, optical bandgap widening, increased lattice disorder, and suppressed non-radiative recombination. However, at higher en^{2+} loading, {en}$MAPbI_3$ transforms to the cubic perovskite phase at room temperature, making it more susceptible to defect-mediated carrier recombination. The tetragonal-to-orthorhombic phase transition temperature of $MAPbI_3$ decreases with increasing en^{2+} content, underscoring the role of MA^+ dipole–dipole interactions in driving structural changes in the inorganic [PbI_6] framework. Additionally, this work identifies the low-temperature broadband PL of $MAPbI_3$ as originating from self-trapped exciton (STE) emission, with the emission peak blueshifting under higher excitation powers. Free excitons induce the realignment of the surrounding MA^+ dipole to achieve a more stable nuclear configuration, resulting in broadband emission with a large Stokes shift. The introduction of en^{2+} at the A-site disrupts MA^+ interactions, reducing the extent of STE stabilization. These findings highlight the critical role of A-site cation dipole dynamics in governing phase transitions and excitonic properties in hybrid halide perovskites. By understanding and controlling these dynamics, {en}$MAPbI_3$ emerges as a promising material with a tuneable optical bandgap and suppressed defect-mediated recombination compared to its parent compound, making it suitable for optoelectronic applications that require stable and tuneable emission properties.

Author contributions

C.-H. Yeh: investigation, formal analysis, visualization, writing – original draft. W.-Y. Cheng: investigation, formal analysis, methodology. T.-C. Chou: methodology, supervision. Y.-C. Liu: methodology, supervision. C.-W. Chang: investigation, methodology. Y.-S. Chen: methodology. C.-H. Wang: methodology, supervision. S.-C. Weng: methodology, resources, supervision. I. D. Sharp: conceptualization, project administration, writing – review & editing. P.-T. Chou: resources, supervision, writing – review & editing. C.-M. Jiang: conceptualization, funding acquisition, project administration, writing – review & editing, data curation.

Conflicts of interest

There are no conflicts to declare.

Data availability

The following data supporting this article have been included as part of the SI.

Fig. S1: Schematic diagram of the spin-coating procedure for synthesizing {en}$MAPbI_3$ films. Fig. S2: PXRD patterns of {en}$MAPbI_3$ films synthesized using different annealing temperatures. Fig. S3 and S4: SEM images of {en}$MAPbI_3$ films. Fig. S5: Temperature-dependent (110) diffraction peak position of pristine $MAPbI_3$. Fig. S6: 10 K PL spectra of {en}$MAPbI_3$ films. Fig. S7: 10 K PL spectra of 7.5% en^{2+} sample measured using different excitation powers. Fig. S8: Comparison of 10 K PL spectra of pristine $MAPbI_3$ and {en}$MAPbI_3$ with 7.5% en^{2+} loading used either a xenon lamp or a 510 nm pulsed laser as the excitation source. See DOI: https://doi.org/10.1039/d5na00599j.

Acknowledgements

This research was financially supported by the National Science and Technology Council under Grant No. MOST 110-2113-M-002-027-MY3, and by the Office of Research and Development, National Taiwan University (NTU) under Grant No. 113L893305. I. D. S. acknowledges support from the Deutsche Forschungsgemeinschaft (DFG, German Research Foundation) under Germany's Excellence Strategy – EXC 2089/1-390776260 and from TUM. solar in the context of the Bavarian Collaborative Research Project Solar Technologies Go Hybrid (SolTech). We thank C.-Y. Chien and S.-J. Ji of the Instrumentation Center at NTU for their assistance in SEM operation.

References

1 T. Chen, W.-L. Chen, B. J. Foley, J. Lee, J. P. Ruff, J. P. Ko, C. M. Brown, L. W. Harriger, D. Zhang and C. Park, *Proc. Natl. Acad. Sci. U. S. A.*, 2017, **114**, 7519–7524.
2 M. A. Green, Y. Jiang, A. M. Soufiani and A. Ho-Baillie, *J. Phys. Chem. Lett.*, 2015, **6**, 4774–4785.
3 J. Xu, A. Maxwell, M. Wei, Z. Wang, B. Chen, T. Zhu and E. H. Sargent, *ACS Energy Lett.*, 2021, **6**, 4220–4227.
4 Y. Zhou, I. Poli, D. Meggiolaro, F. De Angelis and A. Petrozza, *Nat. Rev. Mater.*, 2021, **6**, 986–1002.
5 G. W. Kim and A. Petrozza, *Adv. Energy Mater.*, 2020, **10**, 2001959.
6 M. J. Jeong, C. S. Moon, S. Lee, J. M. Im, M. Y. Woo, J. H. Lee, H. Cho, S. W. Jeon and J. H. Noh, *Joule*, 2023, **7**, 112–127.
7 Q. Jiang, J. Tong, Y. Xian, R. A. Kerner, S. P. Dunfield, C. Xiao, R. A. Scheidt, D. Kuciauskas, X. Wang and M. P. Hautzinger, *Nature*, 2022, **611**, 278–283.
8 Y. Zhao, F. Ma, Z. Qu, S. Yu, T. Shen, H.-X. Deng, X. Chu, X. Peng, Y. Yuan and X. Zhang, *Science*, 2022, **377**, 531–534.
9 B. Zhang, Y. Liao, L. Tong, Y. Yang and X. Wang, *Phys. Chem. Chem. Phys.*, 2020, **22**, 7778–7786.
10 A. F. Akbulatov, S. Y. Luchkin, L. A. Frolova, N. N. Dremova, K. L. Gerasimov, I. S. Zhidkov, D. V. Anokhin, E. Z. Kurmaev, K. J. Stevenson and P. A. Troshin, *J. Phys. Chem. Lett.*, 2017, **8**, 1211–1218.
11 B. w. Park and S. I. Seok, *Adv. Mater.*, 2019, **31**, 1805337.
12 L. Lanzetta, N. Aristidou and S. A. Haque, *J. Phys. Chem. Lett.*, 2020, **11**, 574–585.
13 K. Jayanthi, I. Spanopoulos, N. Zibouche, A. A. Voskanyan, E. S. Vasileiadou, M. S. Islam, A. Navrotsky and M. G. Kanatzidis, *J. Am. Chem. Soc.*, 2022, **144**, 8223–8230.
14 W. Ke, C. C. Stoumpos, M. Zhu, L. Mao, I. Spanopoulos, J. Liu, O. Y. Kontsevoi, M. Chen, D. Sarma, Y. Zhang, M. R. Wasielewski and M. G. Kanatzidis, *Sci. Adv.*, 2017, **3**, e1701293.

15 I. Spanopoulos, I. Hadar, W. Ke, P. Guo, E. M. Mozur, E. Morgan, S. Wang, D. Zheng, S. Padgaonkar, G. N. Manjunatha Reddy, E. A. Weiss, M. C. Hersam, R. Seshadri, R. D. Schaller and M. G. Kanatzidis, *J. Am. Chem. Soc.*, 2021, **143**, 7069–7080.
16 I. Spanopoulos, W. Ke, C. C. Stoumpos, E. C. Schueller, O. Y. Kontsevoi, R. Seshadri and M. G. Kanatzidis, *J. Am. Chem. Soc.*, 2018, **140**, 5728–5742.
17 L. Grater, M. Wang, S. Teale, S. Mahesh, A. Maxwell, Y. Liu, S. M. Park, B. Chen, F. Laquai, M. G. Kanatzidis and E. H. Sargent, *J. Phys. Chem. Lett.*, 2023, **14**, 6157–6162.
18 W. Ke, I. Spanopoulos, Q. Tu, I. Hadar, X. Li, G. S. Shekhawat, V. P. Dravid and M. G. Kanatzidis, *J. Am. Chem. Soc.*, 2019, **141**, 8627–8637.
19 W. Ke, C. C. Stoumpos, I. Spanopoulos, L. Mao, M. Chen, M. R. Wasielewski and M. G. Kanatzidis, *J. Am. Chem. Soc.*, 2017, **139**, 14800–14806.
20 W. Ke, C. C. Stoumpos, I. Spanopoulos, M. Chen, M. R. Wasielewski and M. G. Kanatzidis, *ACS Energy Lett.*, 2018, **3**, 1470–1476.
21 A. Leblanc, N. Mercier, M. Allain, J. Dittmer, V. Fernandez and T. Pauporté, *Angew. Chem., Int. Ed.*, 2017, **56**, 16067–16072.
22 J. Lu, L. Jiang, W. Li, F. Li, N. K. Pai, A. D. Scully, C. M. Tsai, U. Bach, A. N. Simonov and Y. B. Cheng, *Adv. Energy Mater.*, 2017, **7**, 1700444.
23 C.-M. Tsai, Y.-P. Lin, M. K. Pola, S. Narra, E. Jokar, Y.-W. Yang and E. W.-G. Diau, *ACS Energy Lett.*, 2018, **3**, 2077–2085.
24 Y. Fu, M. P. Hautzinger, Z. Luo, F. Wang, D. Pan, M. M. Aristov, I. A. Guzei, A. Pan, X. Zhu and S. Jin, *ACS Cent. Sci.*, 2019, **5**, 1377–1386.
25 X. Li, M. Kepenekian, L. Li, H. Dong, C. C. Stoumpos, R. Seshadri, C. Katan, P. Guo, J. Even and M. G. Kanatzidis, *J. Am. Chem. Soc.*, 2022, **144**, 3902–3912.
26 A. Al-Kahtani, S. Tabassum, I. Raya, I. Khlewee, S. Chupradit, A. Davarpanah, M. Elveny and S. Ali, *Coatings*, 2021, **11**, 1341.
27 S. Maheshwari, M. B. Fridriksson, S. Seal, J. Meyer and F. C. Grozema, *J. Phys. Chem. C*, 2019, **123**, 14652–14661.
28 A. A. Koegel, E. M. Mozur, I. W. Oswald, N. H. Jalarvo, T. R. Prisk, M. Tyagi and J. R. Neilson, *J. Am. Chem. Soc.*, 2022, **144**, 1313–1322.
29 A. Bonadio, F. P. Sabino, A. L. Freitas, M. R. Felez, G. M. Dalpian and J. A. Souza, *Inorg. Chem.*, 2023, **62**, 7533–7544.
30 A. Halder, Y. Rakita, D. Cahen and S. K. Sarkar, *J. Phys. Chem. Lett.*, 2020, **11**, 1473–1476.
31 W. Kong, Z. Ye, Z. Qi, B. Zhang, M. Wang, A. Rahimi-Iman and H. Wu, *Phys. Chem. Chem. Phys.*, 2015, **17**, 16405–16411.
32 Y. Li, H. Song, X. Ma, J. Liu, C. Ge, D. Liu and S. Liu, *J. Phys. Chem. C*, 2023, **127**, 12613–12620.
33 C. Yu, Y. Kawakita, T. Kikuchi, M. Kofu, T. Honda, Z. Zhang, Z. Zhang, Y. Liu, S. F. Liu and B. Li, *J. Phys. Chem. Lett.*, 2024, **15**, 329–338.
34 S. Maheshwari, S. Patwardhan, G. C. Schatz, N. Renaud and F. C. Grozema, *Phys. Chem. Chem. Phys.*, 2019, **21**, 16564–16572.
35 E. M. Mozur, M. A. Hope, J. C. Trowbridge, D. M. Halat, L. L. Daemen, A. E. Maughan, T. R. Prisk, C. P. Grey and J. R. Neilson, *Chem. Mater.*, 2020, **32**, 6266–6277.
36 J. H. Lee, J.-H. Lee, E.-H. Kong and H. M. Jang, *Sci. Rep.*, 2016, **6**, 21687.
37 S. Li, J. Luo, J. Liu and J. Tang, *J. Phys. Chem. Lett.*, 2019, **10**, 1999–2007.
38 Z. Xu, X. Jiang, H.-p. Cai, K. Chen, X. Yao and Y. Feng, *J. Phys. Chem. Lett.*, 2021, **12**, 10472–10478.
39 J. Tan, D. Li, J. Zhu, N. Han, Y. Gong and Y. Zhang, *Nanoscale*, 2022, **14**, 16394–16414.
40 H.-C. Chu, C.-M. Hung, H.-C. Huang, S.-C. Weng, B.-H. Lin, S. Yang, Y.-H. Wu, K.-H. Chang, J.-J. Shyue and P.-T. Chou, *J. Phys. Chem. C*, 2024, **128**, 20441–20450.
41 C. Wu, K. Chen, D. Guo, S. Wang and P. Li, *RSC Adv.*, 2018, **8**, 2900–2905.
42 L. Q. Phuong, Y. Yamada, M. Nagai, N. Maruyama, A. Wakamiya and Y. Kanemitsu, *J. Phys. Chem. Lett.*, 2016, **7**, 2316–2321.
43 Q. Chen, N. De Marco, Y. Yang, T.-B. Song, C.-C. Chen, H. Zhao, Z. Hong, H. Zhou and Y. Yang, *Nano Today*, 2015, **10**, 355.
44 A. A. Baloch, F. H. Alharbi, G. Grancini, M. I. Hossain, M. K. Nazeeruddin and N. Tabet, *J. Phys. Chem. C*, 2018, **122**, 26805–26815.
45 A. D. Wright, C. Verdi, R. L. Milot, G. E. Eperon, M. A. Pérez-Osorio, H. J. Snaith, F. Giustino, M. B. Johnston and L. M. Herz, *Nat. Commun.*, 2016, **7**, 11755.
46 J. A. Steele, P. Puech, M. Keshavarz, R. Yang, S. Banerjee, E. Debroye, C. W. Kim, H. Yuan, N. H. Heo and J. Vanacken, *ACS Nano*, 2018, **12**, 8081–8090.
47 L. M. Herz, *Annu. Rev. Phys. Chem.*, 2016, **67**, 65–89.
48 V. D'innocenzo, G. Grancini, M. J. Alcocer, A. R. S. Kandada, S. D. Stranks, M. M. Lee, G. Lanzani, H. J. Snaith and A. Petrozza, *Nat. Commun.*, 2014, **5**, 3586.
49 F. Ambrosio, E. Mosconi, A. A. Alasmari, F. A. S. Alasmary, D. Meggiolaro and F. De Angelis, *Chem. Mater.*, 2020, **32**, 6916–6924.
50 S. Krishnamurthy, R. Naphade, W. J. Mir, S. Gosavi, S. Chakraborty, R. Vaidhyanathan and S. Ogale, *Adv. Opt. Mater.*, 2018, **6**, 1800751.
51 J. M. Urban, T. H. T. Nguyen, G. Chehade, A. Delteil, G. Trippé-Allard, G. Delport, E. Deleporte, J.-P. Hermier and D. Garrot, *Phys. Status Solidi RRL*, 2023, **17**, 2300005.
52 C. Yang, Q. Wei, Y. Gong, M. Long, G. Zhou, G. Xing and B. Wu, *J. Phys. Chem. Lett.*, 2023, **14**, 10046–10053.
53 J. S. Manser and P. V. Kamat, *Nat. Photon.*, 2014, **8**, 737–743.
54 M. Saba, F. Quochi, A. Mura and G. Bongiovanni, *Acc. Chem. Res.*, 2016, **49**, 166–173.
55 M. I. Dar, G. Jacopin, S. Meloni, A. Mattoni, N. Arora, A. Boziki, S. M. Zakeeruddin, U. Rothlisberger and M. Grätzel, *Sci. Adv.*, 2016, **2**, e1601156.